The k--fP model applied to wind farms

Laan, van der, Paul Maarten; Sørensen, Niels N.; Réthoré, Pierre-Elouan; Mann, Jakob; Kelly, Mark C.; Troldborg, Niels; Hansen, Kurt Schaldemose; Murcia Leon, Juan Pablo

Published in:
Wind Energy

Link to article, DOI:
10.1002/we.1804

Publication date:
2015

Document Version
Early version, also known as pre-print

WIND ENERGY
Wind Energ. 2014; **00**:1–20
DOI: 10.1002/we

RESEARCH ARTICLE

The k-ε-f_P model applied to wind farms

M. Paul van der Laan[1], Niels N. Sørensen[1], Pierre-Elouan Réthoré[1], Jakob Mann[1], Mark C. Kelly[1], Niels Troldborg[1], Kurt S. Hansen[2], Juan P. Murcia[1]

[1]Department of Wind Energy, Technical University of Denmark, Risø campus, DK-4000 Roskilde, Denmark.
[2]Department of Wind Energy, Technical University of Denmark, Lyngby campus, DK-2800 Kgs. Lyngby, Denmark.

ABSTRACT

The recently developed k-ε-f_P eddy-viscosity model is applied to one on-shore and two off-shore wind farms. The results are compared with power measurements and results of the standard the k-ε eddy-viscosity model. In addition, the wind direction uncertainty of the measurements is used to correct the model results with a Gaussian filter. The standard k-ε eddy-viscosity model underpredicts the power deficit of the first downstream wind turbines, whereas the k-ε-f_P eddy-viscosity model shows a good agreement with the measurements. However, the difference in the power deficit predicted by the turbulence models becomes smaller for wind turbines that are a located further downstream. Moreover, the difference between the capability of the turbulence models to estimate the wind farm efficiency, reduces with increasing wind farm size and wind turbine spacing. Copyright © 2014 John Wiley & Sons, Ltd.

KEYWORDS

k-ε eddy viscosity model; wind turbine wake interaction; actuator disc; CFD; RANS; LES; wind direction uncertainty.

Correspondence

M. Paul van der Laan, Department of Wind Energy, Technical University of Denmark, Risø campus, DK-4000 Roskilde, Denmark.
Email: plaa@dtu.dk.

Received ...

1. INTRODUCTION

Wind turbine wakes have a high impact on wind energy production because wake deficits can cause 10% to 20% losses in the annual energy of wind farms [1, 2] and the wake turbulence can decrease the life time of wind turbine blades. It is therefore important to be able to predict the wake effects in wind farms during the design phase. Hence, reliable and relatively fast methods are necessary that can predict wake deficits and wake turbulence. Engineering wake models have shown to be fast, i.e. the N.O. Jensen model [3], however, their accuracy is not always guaranteed [4]. Fuga [5] is a fast linearized Computational Fluid Dynamics (CFD) method that shows good agreement with measurements of wind farms, which is mainly applicable to power predictions but not for wind turbine loads. High fidelity nonlinear Computational Fluid Dynamics (CFD) methods as Large-Eddy Simulation (LES), have proven to produce reliable results in terms of loads and power, that compare well with field measurements [6]. However, LES is an expensive method, that is not suited to predict wake effects in large wind farms for the purpose of wind farm design. Reynolds-Averaged Navier Stokes (RANS), is a nonlinear CFD method that is roughly three orders of magnitude less expensive in computational effort than LES [7]. The reduction in computational effort is achieved by two properties of RANS. First of all, RANS is a steady state calculation, whereas LES is transient. Secondly, RANS requires smaller grid sizes than LES. If the rotor geometry is represented by an actuator disk method [8], one could use a grid around the wind turbine that is uniformly spaced in all directions. In this setup a RANS grid typically needs ten cells to cover a rotor diameter [7], whereas a LES grid can require thirty [9], to resolve the wake accurately. Hence, the RANS grid becomes twenty-seven times smaller than the LES grid. Unfortunately, RANS methods utilize a high level of turbulence modeling, which has proven to dominate the flow solution [10]. A commonly used turbulence model is the k-ε Eddy Viscosity Model (EVM), which is known to underpredict the wake deficit and overpredict the turbulence intensity in the near wake [7, 10, 11, 12, 13]. The problem of the k-ε EVM is related to the fact that the eddy-viscosity coefficient C_μ is a constant. In previous work, the k-ε EVM was extended with a scalar relation for C_μ [7]. The scalar relation, called f_P, is a function of the local shear, which reduces the eddy-viscosity for a

high shear. Since the near wake is characterized by a high local shear, f_P decreases the eddy-viscosity in the near wake and delays the wake recovery. The extended k-ε EVM, hereafter labeled as k-ε-f_P EVM, has been shown to compare well with LES in terms of the velocity deficit of a single wakes [7, 9] and double wakes [14]. In addition, the k-ε-f_P EVM does not overpredict the turbulence intensity in the near wake.

In the current work, the performance of the k-ε-f_P EVM is tested for wind farm simulations. Power measurements from one on-shore and two off-shore wind farms are used to compare with the predicted power of the k-ε-f_P EVM and the original k-ε EVM. The three test cases are described in Section 2. The methodology and the results of the simulations are discussed in Section 3.

2. TEST CASES

The k-ε-f_P EVM and the standard k-ε EVM are applied to three wind farms: the on-shore Wieringermeer wind farm and two off-shore wind farms, Lillgrund and Horns Rev. In total seven test cases are defined and are listed in Table I. The test cases differ in the total ambient turbulence intensity at hub height $I_{H,\infty} \equiv \sqrt{2/3k}/U_{H,\infty}$ (with k as the turbulent kinetic energy), free-stream velocity $U_{H,\infty}$ at hub height $z_{H,\infty}$, rotor diameter D and wind turbine spacing. Note, that the total ambient turbulence intensity is derived from the stream-wise ambient turbulence intensity $I_{H,\infty,u} \equiv \sigma_u/U_{H,\infty}$ that is known from the measurements. Using the ratios of the standard deviations of three velocity components that have been summarized by Panofsky and Dutton [15]:

$$\frac{\sigma_v}{\sigma_u} = 0.8, \qquad \frac{\sigma_w}{\sigma_u} = 0.5, \tag{1}$$

the total ambient turbulence intensity can be written as:

$$I_{H,\infty} = I_{u,H,\infty}\sqrt{\frac{1}{3}\left(1 + 0.8^2 + 0.5^2\right)} \approx 0.8 I_{u,H,\infty}. \tag{2}$$

The first two test cases are derived from the Wieringermeer wind farm that correspond to a low and a high ambient turbulence intensity. Test cases 3 to 6 are based on the Lillgrund wind farm. The Lillgrund test cases differ in wind direction and wind turbine spacing. Cases 3 and 5 correspond to the wind directions that are aligned with the rows, whereas cases 4 and 6 represent wind directions in which the rows are 15°misaligned with respect to the incoming flow. The misaligned cases are referred as the staggered cases. Only one test case is derived from the measurements of the Horns Rev wind farm. The three wind farms are further described in the sections below.

Table I. Summary of cases and corresponding input parameters for numerical computations. wd = wind direction.

Case	Description	Measurement data	$I_{H,\infty}$ ($I_{u,H,\infty}$) [%]	$U_{H,\infty}$ [m/s]	D [m]	z_H [m]	spacing [m/D]
		On-shore wind farm					
1	Wieringermeer, low $I_{H,\infty}$	wd=275°±15°	2.4 (3)	6.59	80	80	3.8
2	Wieringermeer, high $I_{H,\infty}$	wd=275°±15°	9.6 (12)	8.35	80	80	3.8
		Off-shore wind farm					
3	Lillgrund south-west aligned	wd=222°±2.5°, rows B and D	4.8 (6)	9	92.6	65	4.3
4	Lillgrund south-west staggered	wd=207°±2.5°, rows B and D	4.8 (6)	9	92.6	65	
5	Lillgrund south-east aligned	wd=120°±2.5°, rows 4 and 6	4.8 (6)	9	92.6	65	3.2
6	Lillgrund south-east staggered	wd=105°±2.5°, rows 4 and 6	4.8 (6)	9	92.6	65	
7	Horns Rev	wd=270°±2.5°, rows 1-8	5.6 (7)	8	80.0	70	7.0

2.1. On-shore wind farm: Wieringermeer

A row of five wind turbines is located in Wieringermeer, a farmland area in the north west of the Netherlands. The wind turbine row is part of the Wind Turbine Test Site, owned and maintained by ECN. The layout of the five 2.5 MW Nordex N80 wind turbines is sketched in Figure 1. The row is orientated along the 275°wind direction and the spacing between the wind turbines is around 3.8D. The wind turbines have a rotor diameter and hub height of 80 m. Schepers [16] et al. published the results of nearly five years of measurements and the ten minute averaged data is available for the present research. From these measurements, a data set is derived with wind directions of $275^\circ \pm 15^\circ$. A meteorological mast is located south of the wind turbine row and it is used to derive the undisturbed conditions.

Wind Energ. 2014; **00**:1–20 © 2014 John Wiley & Sons, Ltd.
DOI: 10.1002/we
Prepared using weauth.cls

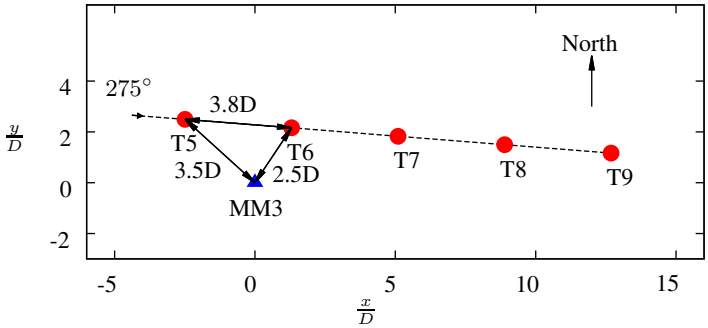

Figure 1. Sketch of wind turbines (red dots) and meteorological mast (blue triangle) at EWTW site.

The power curve and the power coefficient C_P provided by the wind turbine manufacturer is used. The thrust coefficient C_T is not given by Nordex, however, measurements of derived C_T from the tower bending moment and PHATAS [17] calculations of C_T are available from Schepers [18]. The two methods agree well, except for the low wind speeds where the uncertainty in the measured tower bending moment is high. Therefore, the calculated C_T will be used. C_T and C_P are plotted in Figure 2. Only the range of the rotational speed is known: $\Omega = 10.9 - 19.1$ RPM, not the full curve. In order to simulate the wind turbine row in CFD with rotational forces, the full RPM curve as function of the ambient velocity at hub height is necessary. Since the C_P region is relatively flat for wind speeds between 7 and 11 m/s (as indicated by the gray area in Figure 2), it is assumed that the wind turbine starts rotating at the maximum of 19.1 RPM at the end of the flat C_P region (11 m/s), and that the rotational speed is constant up to the cut-out wind speed of 25 m/s. The rotational speed below wind speeds of 11 m/s is derived by assuming a constant Tip Speed Ratio (TSR): $TSR \equiv \Omega(\pi/60)D/U = 7.27$, until the minimum rotational speed of 10.9 RPM is reached at a wind speed of 6.28 m/s. The estimated rotational speed curve is shown in Figure 2.

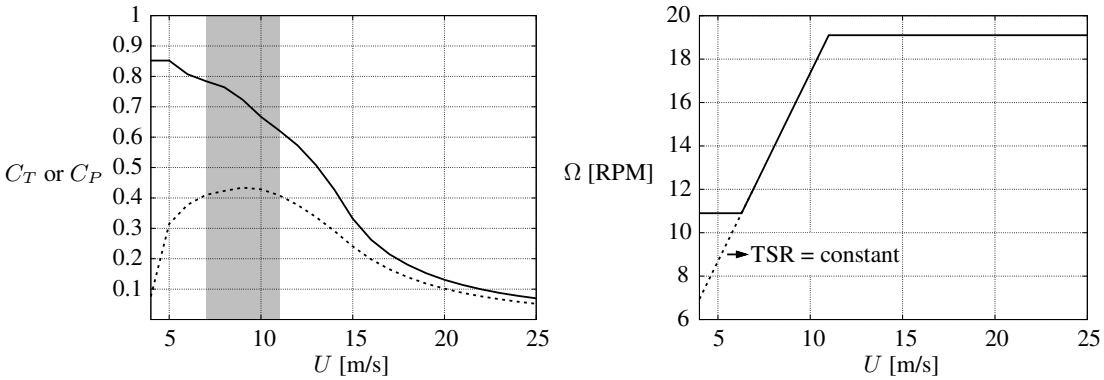

Figure 2. Nordex N80 wind turbine. Left: C_T (solid line) and C_P (dashed line). Gray area indicates the flat C_P region. Right: estimated rotational speed Ω using constant TSR (dashed line).

The meteorological mast is used to calculate the stability from the Monin-Obukhov length L, that is derived from the Bulk Richardson number. This method is described in more detail in the work of Hansen et al. [19]. While bulk-Richardson numbers cannot be reliably used to model the wind field [20, 21], they allow useful classification of stability regimes. Seven stability classes are defined in Table II and the probability of each class is plotted in Figure 3, for cases 1 and 2. In the low ambient turbulence case (case 1), the ABL is stable to very stable, whereas the high ambient turbulence case (case 2) corresponds to near unstable ABL. The present CFD simulations can only model a neutral ABL, hence it should not be expected that the CFD simulations can predict the wake effects in the row of wind turbines for case 1. Nevertheless, case 1 is interesting to investigate how large the disagreement between measurements and simulations is, that is associated with not modeling atmospheric stabilty. Since case 2 is close to neutral, a better agreement between the CFD and the measurements should be expected compared to case 1.

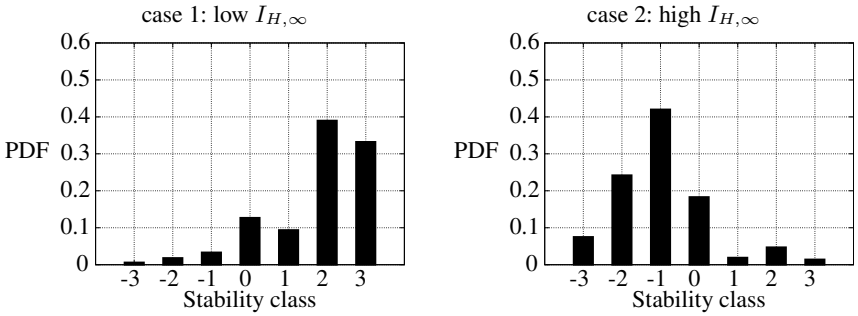

Figure 3. Probability of stability classes for the on-shore wind farm Wieringermeer.

Table II. Definition of stability classes.

Class	Range of L [m]	Description
-3	$-100 \leq L < -50$	Very unstable
-2	$-200 \leq L < -100$	Unstable
-1	$-500 \leq L < -200$	Near unstable
0	$\|L\| > 500$	Neutral
1	$200 \leq L \leq 500$	Near stable
2	$50 \leq L < 200$	Stable
3	$10 \leq L < 50$	Very stable

2.2. Off-shore wind farm: Lillgrund

Lillgrund is an off-shore wind farm, located south of the Øresund bridge that connects Copenhagen (Denmark) with Malmö (Sweden). Figure 4 shows the layout of the off-shore wind farm, which is unique due to the missing wind turbines in the middle of the wind farm. In addition, the wind turbine spacing of 3.2D and 4.3D for the wind direction of 120°and 222°, respectively, is much smaller than the typical spacing of off-shore wind farms that are built today. Note that a spacing of 3.3D is often reported in literature [4, 22, 23, 24], however, a spacing of 300 m is reported in the official drawing of the wind farm layout, which corresponds to a spacing of 3.24D. The narrow spacing is the result of a design change towards maximum power instead of wind farm efficiency, in which larger wind turbines were selected than initially planned, without changing the original layout of the wind farm [22]. Hence, wind turbine wake effects are relatively large in the wind farm (around 30% loss in terms of the annual energy production [22]), which makes it an interesting case to simulate with CFD.

The wind farm includes 48 Siemens SWT-2.3-93 wind turbines that have a rated power of 2.3 MW, a rotor diameter of 92.6 m and a hub height of 65 m. The C_T, C_P and Ω curves are provided by Hansen [23] and are shown in Figure 5. Dahlberg [22] and Hansen [4] derived a measurement set from the SCADA data of Lillgrund. The results of Dahlberg [22] correspond to a data set that is gathered over a period of two years using one-minute bins, in which the yaw positions are not known. Dahlberg assumed zero yaw errors and used the nacelle positions to estimate the wind direction. More recently, Hansen extracted a data set of three years using ten-minute bins, in which the yaw sensors are calibrated against the power deficit peak of a nearby wind turbine, a method that is further described in the work of Barthelmie et al. [25]. Subsequently, the wind direction is derived from the calibrated yaw sensors. The reference wind turbines that are used for determining the wind direction are A5 and C1 for the wind directions 120°and 222°, respectively. The data set of Hansen is chosen in the current research. Unfortunately, the meteorological mast shown in Figure 4 was not available for the period that Hansen used to process the measurements. Therefore, Hansen derived the undisturbed wind speed from the power curve, shown in Figure 5. With this method Hansen selected power data that corresponds to an estimated undisturbed wind speed of 9 ± 0.5 m/s. It should be noted that a group of wind turbines is used to determined the free-stream wind speed, which consists of row 1 and row A for the south-westerly and south-easterly wind directions, respectively. The meteorological mast was erected prior to the wind farm installation, which provides a data set of more than two years. From these measurements Bergström [26] estimated the stream-wise turbulence intensity to be around 6%. The lack of an upstream meteorological mast makes it impossible to investigate the atmospheric stability.

2.3. Off-shore wind farm: Horns Rev

Horns Rev is an off-shore wind farm located 14 km from the West coast of Denmark. The wind farm has a rated power of 160 MW and it consists of 10×8 Vestas V80 wind turbines. The rectangular layout is shown in Figure 6. The wind turbine

Wind Energ. 2014; **00**:1–20 © 2014 John Wiley & Sons, Ltd.
DOI: 10.1002/we
Prepared using weauth.cls

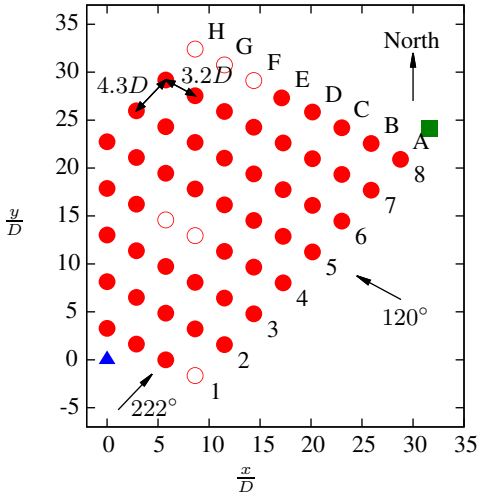

Figure 4. Wind farm layout: wind turbines (red dots), grid position without a wind turbine (red circles), transformer station (green square) and meteorological mast (blue triangle). Distances are normalized with the rotor diameter of the Siemens SWT-2.3-93 wind turbine: $D = 92.6$ m.

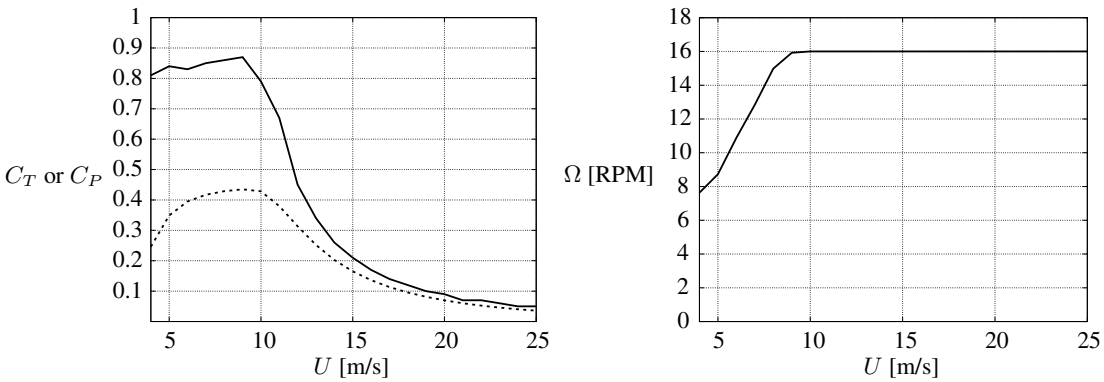

Figure 5. Siemens SWT-2.3-93 wind turbine. Left: C_T (solid line) and C_P (dashed line). Right: rotational speed Ω.

spacing is 7D in the aligned wind directions of 90°-270°and 174°-354°. With a rotor diameter of 80 m, the wind farm fits into a square of dimensions 5.5×4 km^2. The power coefficient, thrust coefficient and the rotational speed of the V80 wind turbine are provided by the Vestas and are shown in Figure 7.

The power measurements for a wind direction of 270°±2.5°and a period between 2005 and 2009 are made available by Hansen and the results are presented in Hansen et al. [19]. Non-neutral atmospheric stability data has been filtered out using the same method as discussed in Section 2.1. Three stability classes are present in the filtered set: near unstable, neutral and near stable. It is found that further reducing the data set, i.e. only allow the neutral class, leads to too few observations.

Unfortunately, the quality of the measurements from meteorological mast M2 shown in Figure 6, is low. Therefore, the free-stream conditions are estimated from wind turbine G1. The wind direction is obtained from the yaw sensor of wind turbine G1, which is calibrated with the power ratio of G2/G1. The free-stream velocity is obtained from power measurements of wind turbine G1 and the power curve from Figure 7.

3. SIMULATIONS

The simulations of the test cases from Table I are discussed in Sections 3.1 and 3.2, in which the method and the results are discussed, respectively.

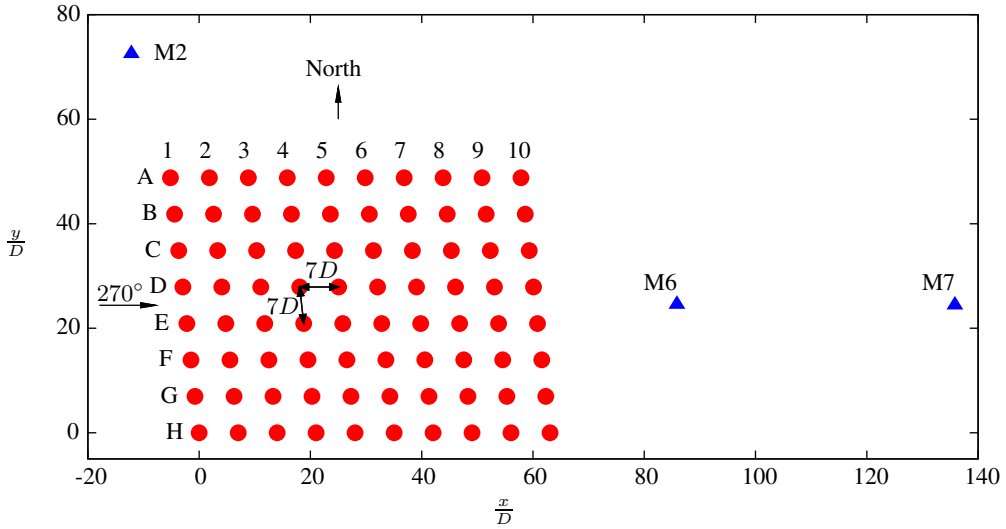

Figure 6. Wind farm layout: wind turbines (red dots) and meteorological masts M2, M6 and M7 (blue triangles). Distances are normalized with the rotor diameter of the Vestas V80 wind turbine: $D = 80$ m.

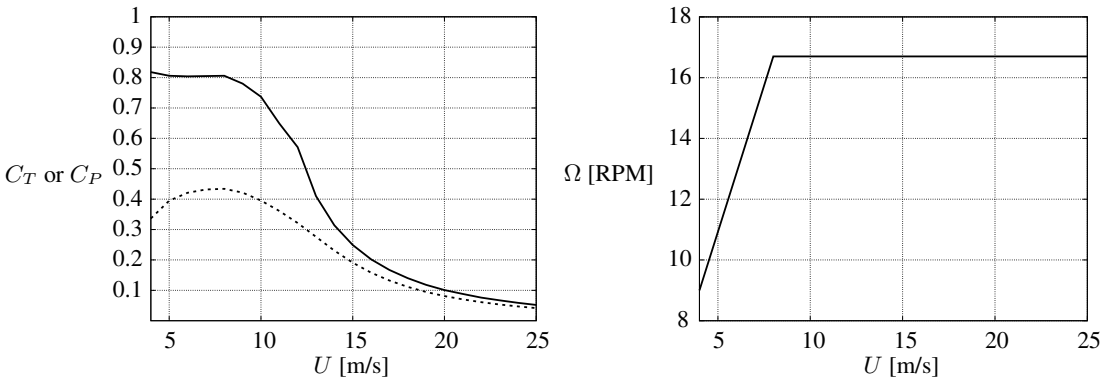

Figure 7. Vestas V80 wind turbine. Left: C_T (solid line) and C_P (dashed line). Right: rotational speed.

3.1. Method

The flow is solved by EllipSys3D, the CFD code of DTU Wind Energy, which is originally developed by Sørensen [27] and Michelsen [28]. The SIMPLE algorithm [29] is chosen to solve the RANS equations. A QUICK scheme [30] is used to discretize convective terms. Since the flow variables are stored in a co-located manner, decoupling of the pressure and body forces can occur. This problem is solved with a modified Rhie-Chow algorithm [31, 32].

The flow domain of the Wieringermeer cases is shown in Figure 8, however, the flow domain definition applies for all cases. A region with a uniform spacing of D/10 in all direction is defined, which is labeled as the wake domain. The cell spacing is based on a grid dependency study of single wind turbine simulations [7]. The wake domain is placed in the center of the flow domain with respect to the xy-plane. Near the wall, at $z = 0$, the cells are refined in the z-direction, towards a first cell height of 0.5 m. The cells are stretched outside the wake domain with a maximum growth ratio of 1.2. The dimension of the flow domain and the wake domain are listed in Table III. The horizontal dimensions of the flow domain that are used for the relatively large wind farms (Lillgrund and Horns Rev), are set to a 1000D, to avoid the influence of the symmetric boundaries at $y = 0$, $y = L_y$ and outlet boundary at $x = L_x$, at which a fully developed flow is assumed. The neutral log law solution is set at the inlet boundaries, located at $x = 0$ and $z = L_z$:

$$U(z) = \frac{u_*}{\kappa} \ln\left(\frac{z}{z_0}\right), \qquad k = \frac{u_*^2}{\sqrt{C_\mu}}, \qquad \varepsilon = \frac{u_*^3}{\kappa z}, \tag{3}$$

where U is the stream-wise velocity, u_* is the friction velocity, $\kappa = 0.4$ is the Von Karman constant, z_0 is the roughness height, k is the turbulent kinetic energy and ε is the turbulent dissipation. The log law solution is retained through out

Wind Energ. 2014; **00**:1–20 © 2014 John Wiley & Sons, Ltd.
DOI: 10.1002/we
Prepared using weauth.cls

the domain by setting a rough wall condition at $z = 0$. At the rough wall, the wall stress and the turbulent dissipation are prescribed, while a Neumann condition is used for the turbulent kinetic energy [33].

It is common to set the ambient turbulence intensity at hub height $I_{H,\infty}$ by changing C_μ in:

$$I_{H,\infty} \equiv \frac{\sqrt{\frac{2}{3}k}}{U_{H,\infty}} = \frac{\kappa\sqrt{\frac{2}{3}}}{\ln\left(\frac{z_H}{z_0}\right)\sqrt[4]{C_\mu}}. \tag{4}$$

However, the f_P function in the k-ε-f_P EVM also changes because it is a function of C_μ, i.e. $f_P = f_P\left(\sigma/\tilde{\sigma}\right)$ and $\tilde{\sigma} = 1/\sqrt{C_\mu}$, with σ as the shear parameter: $\sigma \equiv \frac{k}{\varepsilon}\sqrt{\left(U_{i,j}\right)^2}$ and $\tilde{\sigma}$ as the shear parameter present in the log law solution. In previous work [34], it has been found that the f_P function enhances the wake recovery for higher values of C_μ (corresponding to a lower $I_{H,\infty}$), which is unphysical. To avoid this problem, z_0 is set to obtain the desired $I_{H,\infty}$ through Equation 4, while leaving C_μ constant [7]. Subsequently, the friction velocity is adapted to set the free-stream velocity at hub height $U_{H,\infty}$, using Equation 3. Hence, z_0 and u_* are not based on the field measurements and the resulting simulated velocity profile deviates from the measured velocity profile, however, the differences in the rotor area are small. The maximum difference in velocity in the rotor area between the present method and in a method where the standard off-shore roughness height of 10^{-4} m is used, is less than 0.2% and 2% for the Horns Rev and the Lillgrund cases, respectively. In the Wieringermeer case with low ambient turbulence (case 1), the maximum difference in velocity in the rotor area is 7%, using a field roughness height of 5 cm. This indicates that the low turbulence intensity in case 1 is not caused by the rough wall because the turbulent adapted roughness height z_0 is much smaller than one that is based on the location of the field measurements. It is most likely that the ambient turbulence intensity in case 1 is dominated by the stable atmospheric conditions, as also discussed in Section 2.1 and shown in Figure 3.

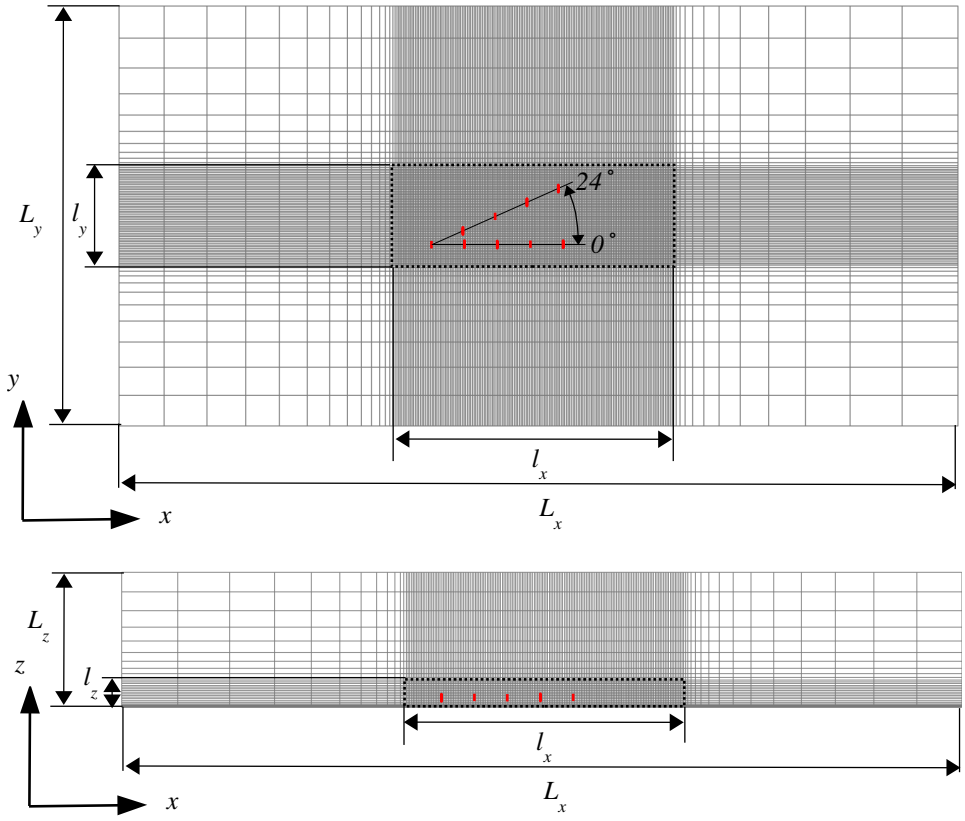

Figure 8. General computational domain. Top: top view. Bottom: side view. Dashed black box marks the wake domain. ADs are illustrated as red boxes. AD setup shown corresponds to test cases 1 and 2. One in every two nodes is shown.

3.1.1. Turbulence models

The standard k-ε EVM from Launder and Spalding [35] and the k-ε-f_P EVM from van der Laan et al. [7] are applied to the wind farm simulations. The turbulence models can only predict isotropic Reynolds-stresses $\overline{u_i' u_j'}$ because the

Table III. RANS flow domain definition of all test cases. Domain sizes are normalized by the rotor diameter D.

		Flow domain			Wake domain			Total number of cells
Case	Description	L_x	L_y	L_z	l_x	l_y	l_z	-
1-2	Wieringermeer	100	50	16	33	11.5	3	3.9×10^6
3-6	Lillgrund	1000	1000	10	55	50	4	2.4×10^7
7	Horns Rev	1000	1000	10	108	102	4	8.5×10^7

Boussinesq approximation [36] is used:

$$\overline{u_i' u_j'} = \frac{2}{3} k \delta_{ij} - \nu_T \left(U_{i,j} + U_{j,i} \right), \tag{5}$$

where δ_{ij} is the Kronecker delta, $U_{i,j}$ are the mean velocity gradients and ν_T is the turbulent eddy viscosity:

$$\nu_T = C_\mu f_P \frac{k^2}{\varepsilon}, \tag{6}$$

with C_μ as a constant and ε as the turbulent dissipation. In the standard k-ε EVM $f_P = 1$ and the effective eddy-viscosity coefficient $C_\mu f_P$ is a constant. In the k-ε-f_P EVM f_P is a scalar function that depends on the local shear parameter: $\sigma \equiv \frac{k}{\varepsilon}\sqrt{(U_{i,j})^2}$. The effective eddy-viscosity coefficient $C_\mu f_P$ is variable, instead of a constant, which is the only difference with the standard k-ε EVM. The scalar function f_P in the k-ε-f_P EVM is defined as:

$$f_P\left(\sigma/\tilde{\sigma}\right) = \frac{2 f_0}{1 + \sqrt{1 + 4 f_0 \left(f_0 - 1\right) \left(\frac{\sigma}{\tilde{\sigma}}\right)^2}}, \; f_0 = \frac{C_R}{C_R - 1}, \tag{7}$$

with $\tilde{\sigma}$ as the shear parameter in an idealized (logarithmic) neutral atmospheric surface layer and C_R is a calibration parameter. In the neutral log law solution $f_P = 1$ because $\sigma = \tilde{\sigma}$. In regions with a high shear parameter, i.e. $\sigma > \tilde{\sigma}$, $f_P < 1$ and the turbulent eddy viscosity from Equation (6) is decreased. The near wind turbine wake is characterized by high velocity gradients, where $\sigma >> \tilde{\sigma}$. As a result, the k-ε-f_P EVM delays the wake recovery compared to the standard k-ε EVM. It should be noted that C_R controls the magnitude of the delayed wake recovery. The constant C_R is calibrated against LES for eight different single wind turbine cases, in previous work [7]. The same transport equations for k and ε are used in both turbulence models:

$$\frac{Dk}{Dt} = \nabla \cdot \left[\left(\nu + \frac{\nu_T}{\sigma_k} \right) \nabla k \right] + \mathcal{P} - \varepsilon, \qquad \frac{D\varepsilon}{Dt} = \nabla \cdot \left[\left(\nu + \frac{\nu_T}{\sigma_\epsilon} \right) \nabla \varepsilon \right] + \left(C_{\varepsilon,1} \mathcal{P} - C_{\varepsilon,2} \varepsilon \right) \frac{\varepsilon}{k}, \tag{8}$$

where $\mathcal{P}$ is the turbulent production, ν is the kinematic molecular viscosity and $C_{\varepsilon,1}, C_{\varepsilon,2}$, σ_k, σ_ε are constants. The values of the constants are listed in Table IV. Note that C_μ is based on atmospheric measurements of Panofsky and Dutton [15], as proposed by Richards and Hoxey [37] and $C_{\varepsilon,1}$ is adapted to maintain the log law solution: $\sqrt{C_\mu}\sigma_\varepsilon \left(C_{\varepsilon,1} - C_{\varepsilon,2} \right) + \kappa^2 = 0$.

Table IV. Model constants.

C_R	C_μ	$C_{\varepsilon,1}$	$C_{\varepsilon,2}$	σ_k	σ_ε	κ
4.5	0.03	1.21	1.92	1.00	1.30	0.40

3.1.2. Wind turbine modeling

The wind turbine geometry is not modeled in the grid. Instead, the Actuator Disk (AD) method [8, 10, 38] is employed to model wind turbine forces. The AD extracts momentum from the Navier-Stokes equations by the addition of a momentum sink. Troldborg et al. [39] showed that the difference in wake flow between a full rotor simulation and an AD simulation is negligible, as long as inflow turbulence is present. In the current work, the AD forces are modeled with the AD Variable Scaling Method, as described in van der Laan et al. [14]. The AD Variable Scaling Method is suited to model the AD forces of interacting wind turbines because the AD forces are a function of local AD velocity. The method uses reference blade force distributions, which are statically scaled with the rotor diameter. In addition, the reference blade force distributions are dynamically scaled during the simulation, with the local AD velocity averaged over the rotor disk $\langle U_{AD} \rangle$, and with calibrated scaling coefficients C_T^*, C_P^* and Ω^*. These scaling coefficients correspond to the thrust coefficient C_T, the

DOI: 10.1002/we
Prepared using weauth.cls

power coefficient C_P and the rotational speed Ω, respectively, as function of $\langle U_{AD} \rangle$. The relationship of C_T^*, C_P^* and Ω^* with $\langle U_{AD} \rangle$ is derived from a calibration procedure, in which a number of single AD simulations are carried out, that corresponds to a range of free-stream velocities, e.g. between 4-25 m/s with a uniform spacing of 1 m/s. Assuming that C_T, C_P and Ω are known as function of the free-stream velocity, the total AD forces in each single wind turbine simulation is prescribed and $\langle U_{AD} \rangle$ can be extracted from the converged solution.

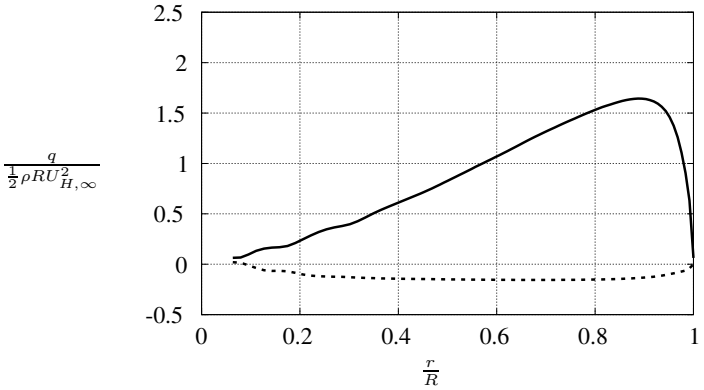

Figure 9. Calculated tangential q_T (dashed line) and normal force q_N (solid line) distributions [n/m].

In the present work, the calibration procedure is carried out for the following wind turbines: N80, SWT-2.3-93 and V80. The blade force distributions from a full rotor detached-eddy simulation of the NREL-5MW wind turbine are used as the reference blade force distributions, that are scaled as mentioned previously. The results for the normal and the tangential force distribution are plotted in Figure 9. The numerical setup for the single wind turbine simulations is described in detail in the work of van der Laan et al. [7]. The calibration procedure is repeated whenever the turbulence model or the ambient turbulence intensity is changed. The calibration of the Nordex N80 wind turbine from Section 2.1 is shown in Figure 10. The calibrated scaling coefficients C_T^*, C_P^* and Ω^* are plotted as function of the averaged AD velocity $\langle U_{AD} \rangle$. Four different calibrations are given that differ in turbulence model and ambient turbulence intensity. C_T^* and C_P^* show sensitivity to the turbulence model and ambient turbulent intensity, in the low wind speed range, as also observed in previous work [14]. The sensitivity in turbulence model is caused by the fact that the k-ε EVM underpredicts the induction compared to LES, whereas the k-ε-f_P EVM predicts a correct induction. Therefore, it is important to redo the calibration if the turbulence model or the ambient turbulence intensity is changed. The calibration results of the other wind turbines are not given in the paper.

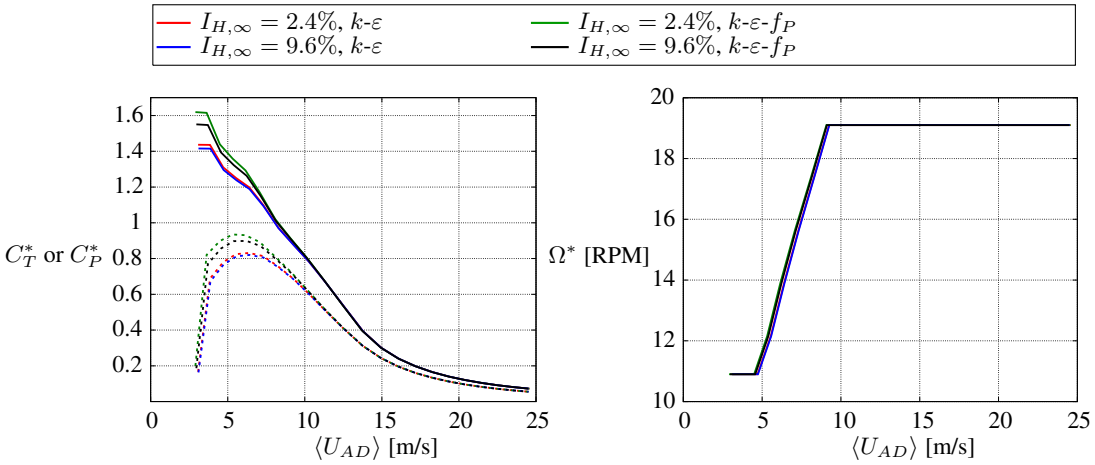

Figure 10. Nordex N80 wind turbine. Left: C_T^* (solid line) and C_P^* (dashed line). Right: rotational speed Ω^* in RPM.

3.1.3. Post processing for measurement uncertainty of the wind direction

Gaumond et al. [40] showed that the wind direction uncertainty is large in measurements that are processed with narrow wind direction bins. As a result, the measured power deficit decreases for a narrow wind direction bin that is aligned with

the wind turbine rows, because power measurements outside the wind direction bin, which corresponds to partial or no wake conditions, are also included. Gaumond et al. argued to correct model results for wind direction uncertainty, such that a fair comparison with measurements can be made. Three sources of the wind direction uncertainty are identified by Gaumond et al.:

1. The use of a yaw sensor to obtain the wind direction, instead of a direct measurement, i.e. a wind vane.
2. The spatial decorrelation of the reference wind direction measurement with respect to the undisturbed wind direction that is present far away from the reference location.
3. The change in wind direction due to large scale turbulence that is statistically not well represented within ten minute averages.

In the present work, the first two sources of wind direction uncertainty are estimated for the Horns Rev wind farm by investigating the standard deviation of the difference in the wind direction that is measured with a wind vane at the meteorological mast M2 $\theta_{\mathrm{M2,i}}$ with the wind direction that is computed from the yaw sensors $\theta_{\mathrm{yaw,i}}$:

$$\Delta\theta_{\mathrm{i}} = \theta_{\mathrm{yaw,i}} - \theta_{\mathrm{M2,i}} \tag{9}$$

Note that the meteorological mast M2 is located 2km north from the Horns Rev wind farm, as shown in Figure 6, and was only partly available during the period of the power measurements. In Figure 11, the standard deviation of $\Delta\theta_{\mathrm{i}}$ is plotted against the distance between M2 and the individual wind turbines ΔL. The data collapses to a linear curve:

$$\sigma_{\Delta\theta} = 3.5 \times 10^{-4}\Delta L + 2.1. \tag{10}$$

Figure 11 indicates that the wind direction uncertainty increases linearly with the distance from the reference location. In addition, even if M2 was placed at the location of the yaw sensor, still a difference in standard deviation of 2.1° is predicted. In other words, the standard deviation of the wind direction is increased by 2.1° because a yaw sensor is used to measure the wind direction, instead of a wind vane.

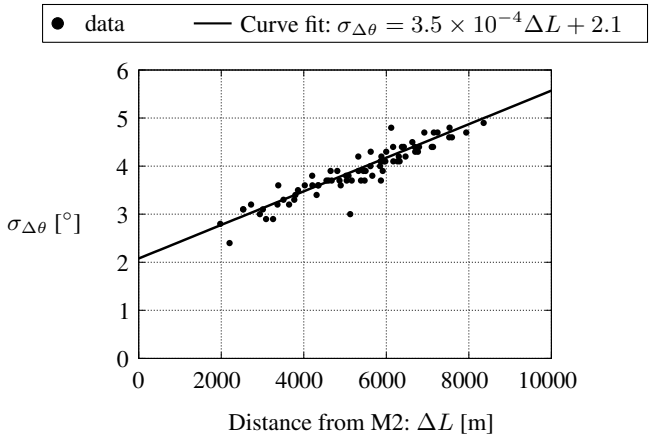

Figure 11. Difference in standard deviation beteen meteorological mast M2 and the yaw sensors of the wind turbines in Horns Rev.

Ott and Nielsen [5] argued that the wind direction uncertainty, associated with the large scale turbulence that is statistically not well represented within ten minute averages: σ_{lst}, can be estimated from the difference in consecutive ten minute averaged wind direction measurements. This idea is adapted in the present work, using all three meteorological masts at Horns Rev: M2, M6 and M7, as shown in Figure 6. For M2, σ_{lst} is obtained from a Gaussian fit of the distribution $\Delta\theta_{\mathrm{M2,i}}$:

$$\Delta\theta_{\mathrm{M2,i}} = \theta_{\mathrm{M2,i+1}} - \theta_{\mathrm{M2,i}}, \tag{11}$$

using the consecutive wind direction measurements $\theta_{\mathrm{M2,i}}$ and $\theta_{\mathrm{M2,i+1}}$. The data is filtered for outliers before the Gaussian fit is performed. The final results of the unfiltered distribution and the Gaussian fit for M2 is plotted in Figure 12. The exercise is repeated for M6 and M7 and the results for σ_{lst} are listed in Table V.

We assume that all three sources of wind direction uncertainty can be written as a single standard deviation σ_{total}:

$$\sigma_{\mathrm{total}} = \sqrt{\sigma_{\Delta\theta}^2 + \sigma_{\mathrm{lst}}^2}. \tag{12}$$

The average result for σ_{lst} is used (2.5°), as listed in Table V.

Wind Energ. 2014; **00**:1–20 © 2014 John Wiley & Sons, Ltd.
DOI: 10.1002/we
Prepared using weauth.cls

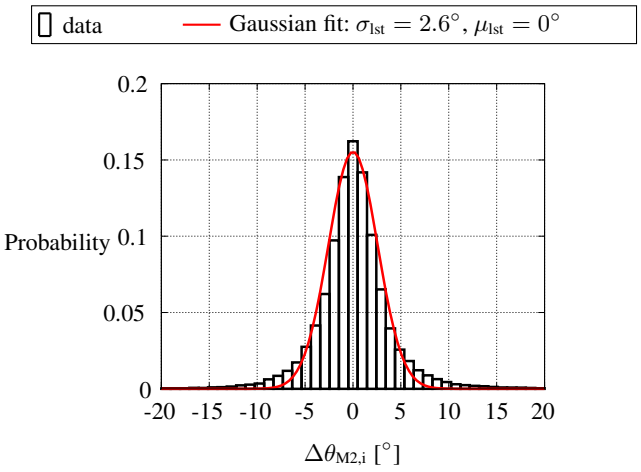

Figure 12. The difference of consecutive ten minute wind direction averages measured at meteorological mast M2.

Table V. Estimation of σ_{lst} for three different meteorological mast at Horns Rev.

Meteorological mast	M2	M6	M7	Average
σ_{lst} [°]	2.6	2.5	2.5	2.5

It is believed that the wind direction uncertainty in the Lillgrund and Wieringermeer wind farms is lower than the Horns Rev wind farm because both the Lillgrund and Wieringermeer wind farms are much smaller than Horns Rev. Since the wind direction in the Lillgrund wind farm is still based on yaw sensors, it is assumed that the standard deviation in wind direction due to using yaw sensors is 2.1°, i.e. substituting $\Delta L = 0$ in Equation (10). The effect of decorrelation is neglected because the reference wind turbine that is used to obtain the wind direction, is always the first wind turbine in a neighboring row with respect to the rows of the Lillgrund test cases (i.e A5 for row 4 and 6, and C1 for row B and D). In other words, the distance of the measured power deficits and the reference wind turbine is small. The Wieringermeer wind farm uses wind vanes that are positioned at a nearby meteorological mast, hence the wind direction uncertainty due to using a yaw sensor can be neglected. The estimated wind direction uncertainty per wind farm is summarized in Table VI.

Table VI. Estimated wind direction uncertainty of the measurements.

		Wind direction uncertainty in terms of σ [°]			
Case	Description	Decorrelation	Yaw sensors	Large scale turb.	Total
1-2	Wieringermeer	-	-	2.5	2.5
3-6	Lillgrund	-	2.1	2.5	3.3
7	Horns Rev	$3.5 \times 10^{-4}\Delta L + 2.1$		2.5	$\sqrt{(3.5 \times 10^{-4}\Delta L + 2.1)^2 + 2.5^2}$

The three sources of wind direction uncertainty are taken into account by averaging the simulated wind directions with a Gaussian filter [40], in which the standard deviation is based on total standard deviation listed in Table VI. The Gaussian averaging is performed over an interval of $\pm 3\sigma_{total}$ such that 99.7% of the Gaussian filter is applied.

3.2. Results and Discussion

The results of the on-shore Wieringermeer wind farm and the two off-shore wind farms Lillgrund and Horns Rev, are discussed separately in the proceeding sections. In all power deficit plots, two results for each RANS turbulence model are shown; the solid line represents the result of each single wind direction and the dashed line is the post-processed result of a Gaussian average using an interval of $\pm 3\sigma_{total}$. This Gaussian averaging represents the wind direction uncertainty that is typically observed in measurements that are processed with narrow wind direction bins, as explained in Section 3.1.3. The wind farm efficiency of all test cases is evaluated in Section 3.2.4.

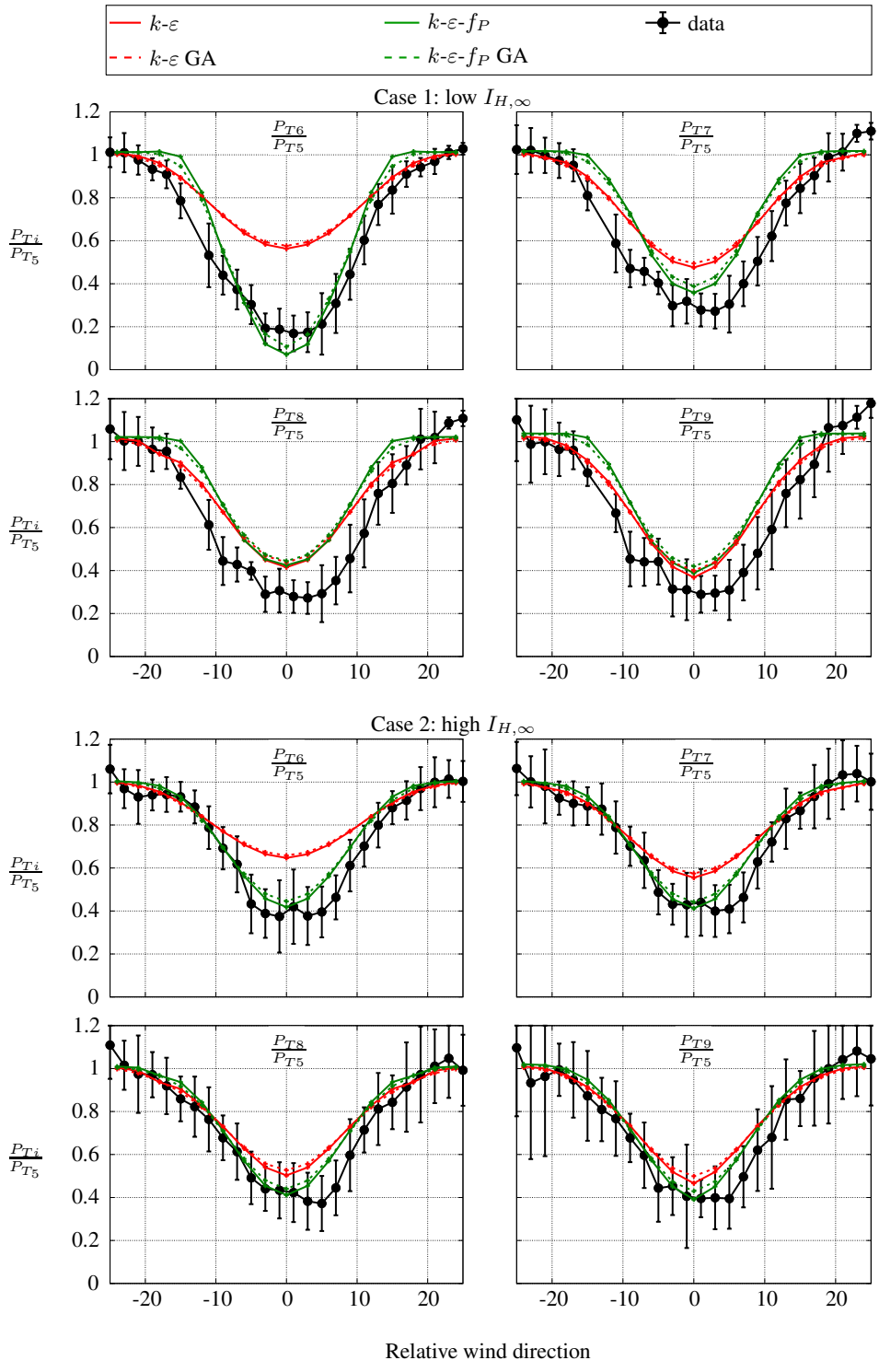

Figure 13. Power deficit in the Wieringermeer wind farm as function of wind direction. Measurements include error bars of one standard deviation. Solid and dashed lines: solution without and with Gaussian averaging (GA), respectively.

3.2.1. Wieringermeer

In Figure 13, the power deficit is plotted as function of westerly wind directions for each of the four downstream wind turbines (T6, T7, T8 and T9) separately, for low and high ambient turbulence intensities (cases 1 and 2 of Table I). The

Wind Energ. 2014; **00**:1–20 © 2014 John Wiley & Sons, Ltd.
DOI: 10.1002/we
Prepared using weauth.cls

power deficit of each wind turbine is normalized by the first turbine in the row (T5). The numerical computations using the standard k-ε EVM and k-ε-f_P EVM are carried out for relative wind directions between 0°and 24°, with a constant interval of 3°. The results of the negative relative wind direction range (-24°to 0°) is the mirror image of the results of the positive relative wind directions. Hence, the effect of rotation on the power deficit is assumed to be negligible. This assumption is tested at the end of the present section. The Gaussian averaged results, indicated with the dashed lines, are computed using an interval of $\pm 3\sigma_{\text{total}}$ with a standard deviation σ_{total} of 2.5°, as motivated in Section 3.1.3. The power deficits are compared with measurements from Wieringermeer [16], as described Section 2. In case 1, the measured power deficit of the second wind turbine (T6) is very large due to the low ambient turbulence of 2.4%. The calculated power deficit predicted by the k-ε-f_P EVM is even larger than the measured one, however, the power deficit becomes more comparable when the wind direction uncertainty is taken into account. Further downstream, the k-ε-f_P EVM underpredicts the power deficit compared to the measurements. In addition, the measured width of the power deficit is larger than the calculated one. Figure 3 from Section 2.1 shows that the low ambient turbulence in the measurements is caused by very stable atmospheric conditions, which are not modeled in the current RANS simulations. A stable ABL suppresses the generation of wake turbulence and it delays wake recovery, which increases the power deficit. Hence, the stability is a plausible cause for the difference between the measured and the calculated power deficit.

The standard k-ε EVM is known to underpredict the velocity deficit in the near wake [7, 10, 11, 12, 13]. The underpredicted velocity wake deficit translates to an overprediction of the power of the second wind turbine in case 1 by 40%, at a relative wind direction of 0. The difference between the standard k-ε EVM and the k-ε-f_P EVM becomes smaller at the third wind turbine (T7) and further downstream the turbulence models predict similar power deficits. This effect is caused by the increasing turbulence intensity in the (merged) wakes because the single wake simulations have shown, that the difference between the RANS turbulence models is small, when a high ambient turbulence intensity is set at the inlet [7]. In addition, an other mechanism minimizes the difference between the turbulence models in terms of the power deficit of the wind turbines further downstream in the row. Since the k-ε EVM is overpredicting the wake recovery of the first wind turbine wake, the second wind turbine experiences larger forces and its corresponding wake deficit is compensated. Hence, the difference in forcing of the second wind turbine, results in a smaller difference between the turbulence models, in terms of power deficit of the third wind turbine in the row.

In case 2, the ambient turbulence intensity is four times higher than in case 1. The power deficits predicted by the k-ε-f_P EVM is in reasonable agreement with the measurements. The influence of the Gaussian averaging is small because the wind direction uncertainty is estimated to be low. In addition, the difference between the standard k-ε EVM and the k-ε-f_P EVM, in terms of the power deficit of the second wind turbine, is smaller than observed in case 1 because of the higher ambient turbulence intensity.

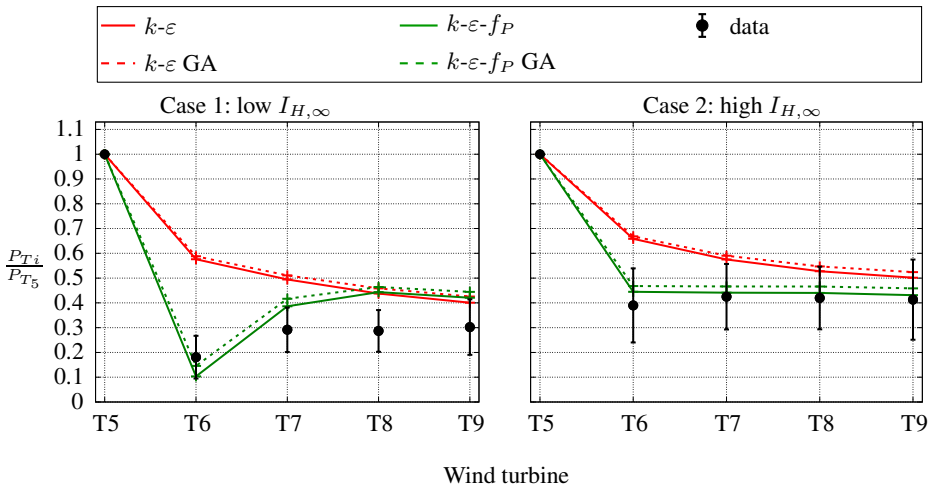

Figure 14. Power deficit in the Wieringermeer wind farm for a wind direction of 275°±3°. Measurements include error bars of one standard deviation. Solid and dashed lines: solution without and with Gaussian averaging (GA), respectively.

A linear averaged power deficit is shown in Figure 14 for the low and high ambient turbulence cases. The measured average consist of three bins between relative wind directions of -3°and 3°, and the average from the simulations represents three simulations corresponding to relative wind direction of -3°, 0°and 3°. Figure 14 emphasizes the statements that the standard k-ε EVM significantly underpredicts the power deficit at the second wind turbine, the k-ε-f_P EVM compares much better with the measurements and both turbulence models show an underpredicted power deficit for the further downstream wind turbines for case 1. Figure 14 also shows that the measured power deficit in case 2 has almost already

reached its asymptotic value at the second wind turbine, since the power deficit does not change much at the other downstream wind turbines. In other words, the momentum loss caused by wake effects, is not further increased when going downstream in the row, because it is in equilibrium with the transport of fresh momentum coming from the undisturbed flow.

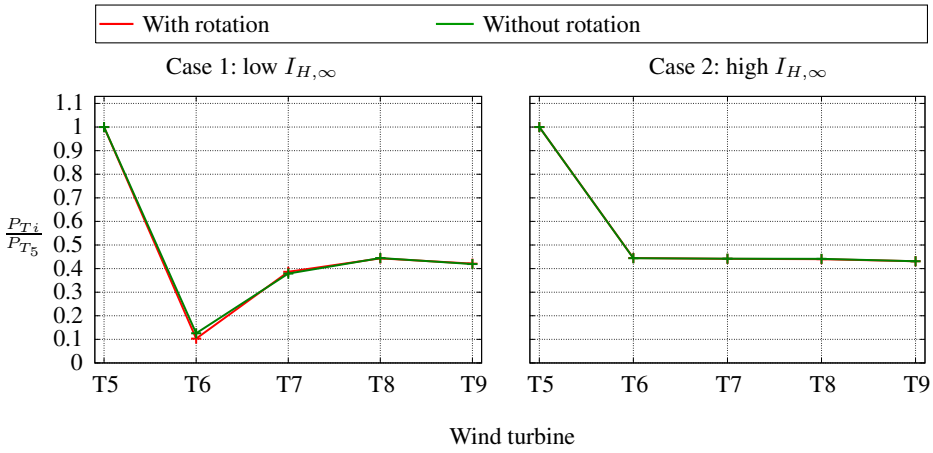

Figure 15. Effect of rotational forces on power deficit in the Wieringermeer wind farm for a wind direction of 275° ±3°.

The effect of the rotational forces is shown in Figure 15, in which the power deficit is plotted with and without rotational forces. Only the k-ε-f_P EVM is used in the comparison and for the simulations without rotational forces a recalibrated C_T^* is used to scale the reference thrust force distribution. Hence, the two methods would predict the same power when they are applied to a single wind turbine simulation. Figure 15 shows that there is a very weak influence of the rotational force on the power deficit. This observation is in contradiction with the work of Wu and Porté-Agel [41], who argued that the rotational forces do influence the power deficit in their LES AD computations of the Horns Rev wind farm. However, Wu and Porté-Agel used different methods to represent the variable forces in the LES simulation with (ADM-R) and without rotation (ADM-NR), which may have led to an unfair comparison. In the ADM-R simulation the forces were based on tabulated airfoil data, as introduced by Sørensen and Shen [42]. The ADM-NR simulations were carried out by a uniformly distributed AD, where the total force is based on a variable thrust force coefficient, using the thrust curve and a local free-stream velocity $U_{H,\infty}$, that is estimated from the local induction factor a_x and an averaged velocity at the AD $\langle U_{AD} \rangle$: $U_{H,\infty} = \langle U_{AD} \rangle / (1 - a_x)$. This method leads to an overprediction of the power, because the free-stream velocity is overestimated, as shown in van der Laan et al. [14]. Hence, the difference between ADM-R and ADM-NR in terms of power deficit is most likely caused by the difference in AD force method, rather than the effect of wake rotation.

3.2.2. Lillgrund

The results of four wind directions, corresponding to the four wind farm cases of Table I, are shown in Figure 16. For each case the power deficit of two rows are plotted; rows B and D for cases 3 and 4 and rows 6 and 4 for cases 5 and 6, respectively. Rows D and 4 are rows where one and two wind turbines are missing. Cases 3 and 5 correspond to wind directions that are aligned with the rows, whereas cases 4 and 6 represent a staggered layout in which the wind directions are 15°misaligned with the direction of the rows. All plots in Figure 16 include results of the standard k-ε EVM and the k-ε-f_P EVM. For both models two results are shown; the power deficit without Gaussian averaging (solid line) and with Gaussian averaging (dashed line). The Gaussian averaging represents the wind direction uncertainty and it is performed over an interval of $\pm 3\sigma_{\text{total}}$ with $\sigma_{\text{total}} = 3.3°$, as discussed in Section 3.1.3. The RANS based models are Gaussian averaged using seven relative wind directions between -15°,15°, with uniform interval of 5°. In addition, the LES results of Churchfield et al. [24] are included for case 3, which corresponds to a single high fidelity simulation. Note that the LES data from Churchfield et al. is renormalized with the power of the first wind turbine, such that a comparison can be made with the results of the RANS models. The wind direction uncertainty is not taken into account in the LES data from Churchfield et al. because only one wind direction was simulated.

First, the Gaussian averaged results are discussed. In all aligned cases (cases 3 and 5), the standard k-ε EVM is not able to predict the measured power deficit of the second wind turbine, whereas the k-ε-f_P EVM shows favorable results. In addition, all cases show that the power deficit calculated by the k-ε EVM approaches the one of k-ε-f_P EVM when going downstream. These two observations were also made in the results of the on-shore wind farm Wieringermeer, in Section 3.2.1. In one of the staggered cases (case 4), both the k-ε EVM and the k-ε-f_P EVM underpredicts the measured power deficit, especially for row B. The two downstream wind turbines in row B do not experience large wake effects in

Wind Energ. 2014; **00**:1–20 © 2014 John Wiley & Sons, Ltd.
DOI: 10.1002/we
Prepared using weauth.cls

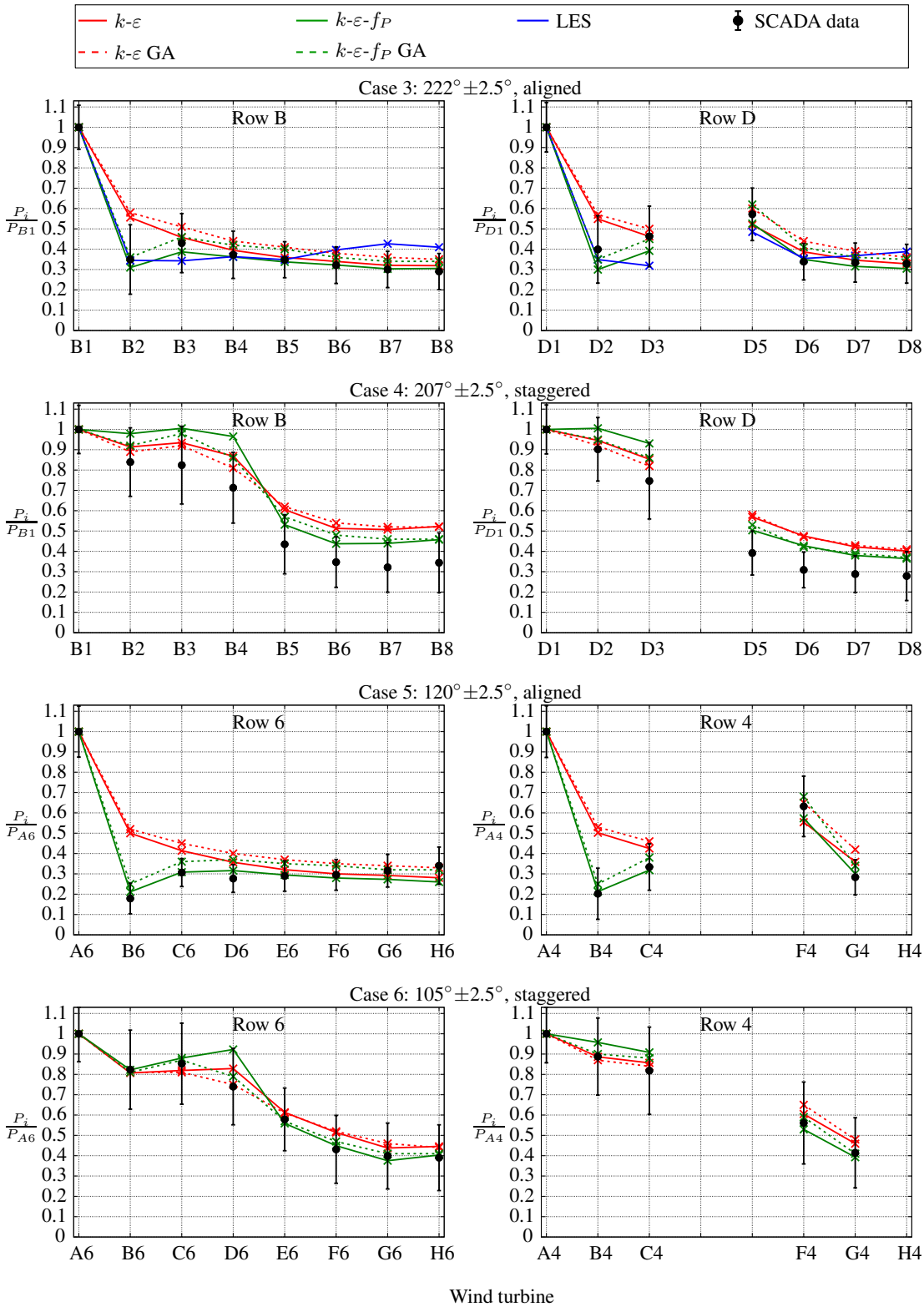

Figure 16. Power deficit in rows in the Lillgrund wind farm for aligned flow directions. LES from Churchfield [24]. Dashed lines include Gaussian averaging (GA).

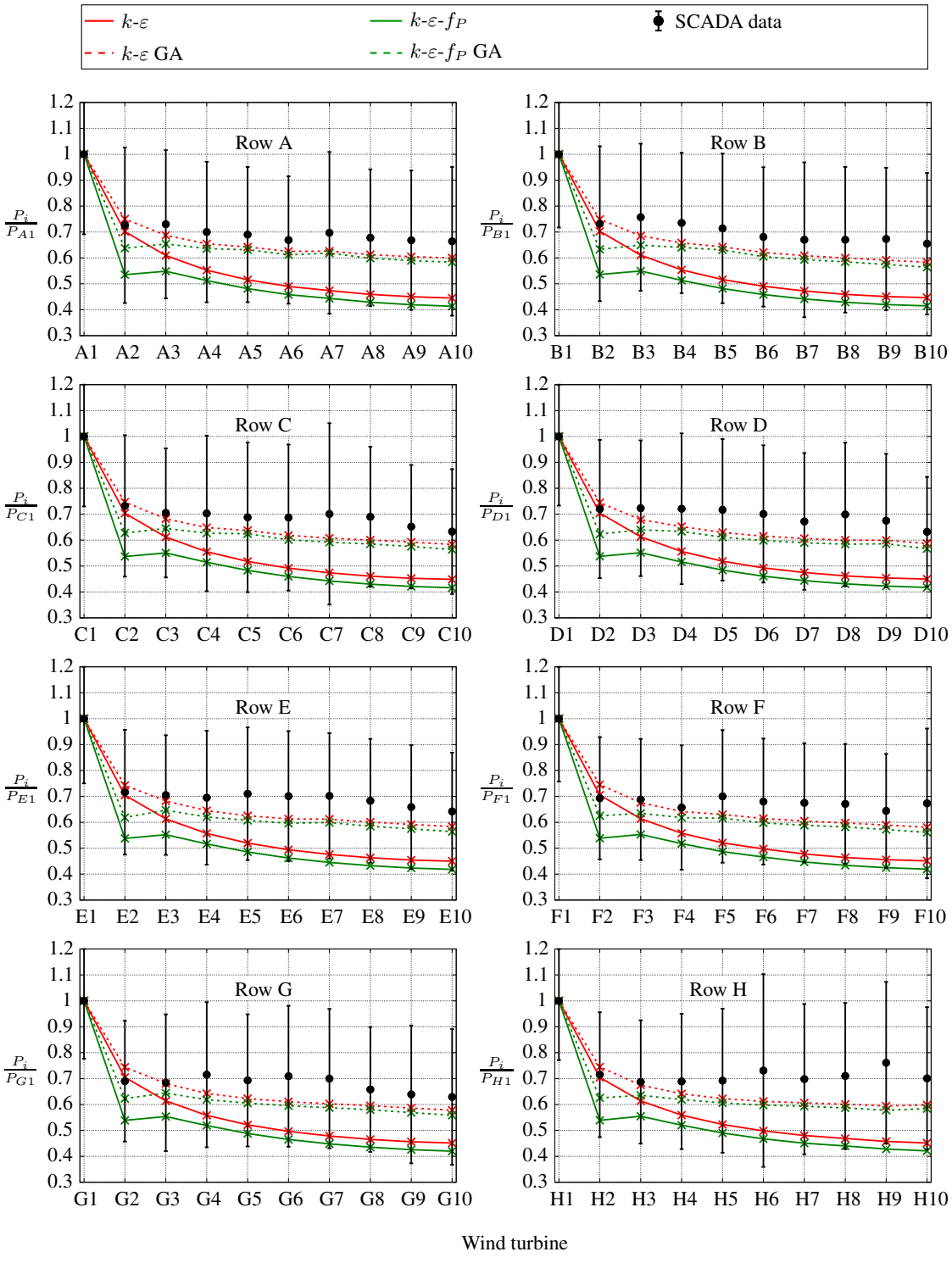

Figure 17. Power deficit in rows in the Horns Rev wind farm for a wind direction of $270^\circ \pm 2.5^\circ$. Dashed lines include Gaussian averaging (GA).

the simulations for a wind direction of 207°, because the upstream wake does not hit the two downstream wind turbines. This is effect is more pronounced in the k-ε-f_P EVM because the standard k-ε EVM has too wide wakes, as observed in single wind turbine simulation in previous work [7]. It is plausible that the uncertainty of the wind direction is larger

Wind Energ. 2014; **00**:1–20 © 2014 John Wiley & Sons, Ltd.
DOI: 10.1002/we
Prepared using weauth.cls

for case 4, although further downstream in rows B and D, the simulated power deficit of the wind turbines will not be improved by a Gaussian filter with a larger standard deviation.

In general, the Gaussian averaging improves the results of the k-ε-f_P EVM. However, the measured power deficit of the second wind turbine of case 5 is best predicted without Gaussian averaging.

Comparing the available LES results with the measurements and other models for case 3, shows that the LES predicts a reasonable wake deficit for row B. However, the LES underpredicts the asymptotic value of the power deficit, as also noted by Churchfield et al. [24]. The LES overpredicts the power deficit in row D for the upstream turbine of the gap and the asymptotic value is again not reached. The reasons for these differences are not clear. One should keep in mind that only one LES simulation is shown (without the Gaussian averaging), which makes it difficult to compare with measurements that include wind direction uncertainty.

3.2.3. Horns Rev

The measured power deficit in the Horns Rev wind farm is plotted in Figure 17 for all eight rows, for a wind direction of $270^\circ \pm 2.5^\circ$. The measured power deficit is compared with two results of the k-ε EVM and the k-ε-f_P EVM, where the dashed and solid lines represents the power deficit with and without Gaussian averaging. The Gaussian averaging is meant to include the wind direction uncertainty of the measurements in the simulations, as discussed in Section 3.1.3. The variable standard deviation of the wind direction uncertainty from Table VI is applied. In order to perform the Gaussian averaging over an interval of $\pm 3\sigma_{\text{total}}$, nine different wind directions are simulated per turbulence model, covering a wind direction range of 250°-290°, with a uniform interval of 5°. Without the Gaussian filter, the power deficit of the second wind turbine, calculated by the k-ε-f_P EVM, is overpredicted in all rows. When the results are Gaussian averaged, the measured power deficit of the second wind turbine and the one calculated by the k-ε-f_P EVM compare better, but there is still an overprediction that continues to exist for the wind turbines further downstream. Possibly, the wind direction uncertainty is higher than estimated in Section 3.1.3. In addition, the Gaussian averaged results would improve if the wind direction uncertainty of Gaumond et al. [40] is applied. Gaumond et al. used a row specific σ_{total}, that is obtained from fitting the power deficit of each second wind turbine in a row, predicted by Fuga [5], to the measurements. This shows that the results are very sensitive to the estimation of the wind direction uncertainty.

It should be noted that the standard deviation of the power measurements is almost twice as high as the data set that includes all atmospheric stability classes. This is not understood because it is expected that the variability of the measurement would decrease when non-neutral atmospheric stability data is filtered out. Note that the average number of observations per wind turbine is 45, which is believed to be sufficient.

As seen in the other test cases, the k-ε EVM predicts a lower power deficit compared the k-ε-f_P EVM, for the second wind turbine in each row, although the difference is not as large as seen in the Lillgrund wind farm (Figure 16). This is caused by the larger wind turbine spacing in Horns Rev (7D) compared to the one in the Lillgrund wind farm (3.2D-4.3D). From the third wind turbine in the row and further downstream, the difference between the turbulence models is negligible.

3.2.4. Wind farm efficiency

The wind farm efficiency is defined as the total power of the wind farm normalized by the power of a single wind turbine without wake effects and the number of wind turbines. In Figure 18, the wind farm efficiency is plotted for all test cases employing the k-ε EVM and k-ε-f_P EVM and the results are compared with the measurements. Note that the wind farm efficiency is only computed for the simulated wind directions, which does not cover the full wind rose. Results with and without Gaussian averaging are shown with the non-filled and filled symbols, respectively. In the first Wieringermeer case, the calculated wind farm efficiencies do not compare well with the measurements, because the effect of atmospheric stability is not modeled. The second Wieringermeer case corresponds to a data set that is measured in near neutral ABL conditions. The k-ε-f_P EVM compares well with the measurements in this test case, whereas, the k-ε EVM overpredicts the measured wind farm efficiency. In the Lillgrund cases (cases 3 to 6), the results of the k-ε EVM and the k-ε-f_P EVM, are reasonably close to the measured values. The effect of Gaussian averaging in the Wieringermeer and Lillgrund cases is small. However, the Gaussian averaging improves the results significantly in the Horns Rev test case (case 7). In addition, the difference between the two turbulence models is negligible. The Horn Rev test case shows that the effect of Gaussian averaging is larger than the difference in wind farm efficiency between the two turbulence models. This indicates that the post processing of the CFD results is just as important as the choice of turbulence model.

The difference in wind farm efficiency between the k-ε EVM and the k-ε-f_P EVM becomes smaller with increasing wind farm size and wind turbine spacing. In the Wieringermeer cases (5 wind turbines, with 3.8D spacing), the aligned Lillgrund case (48 wind turbines, with 3.2D-4.3D spacing) and the Horns Rev wind farm (80 wind turbines, with 7D spacing), the difference in wind farm efficiency without Gaussian averaging is 0.10-0.11, 0.05-0.07, 0.04, respectively. In addition, for wind direction that correspond to staggered configurations, the difference in wind farm efficiency is negligible, as observed in the staggered Lillgrund cases 4 and 6. In other words, if the annual energy of a large wind farm needs to be calculated, the standard k-ε EVM will show a similar performance as the k-ε-f_P EVM, because the complete wind rose

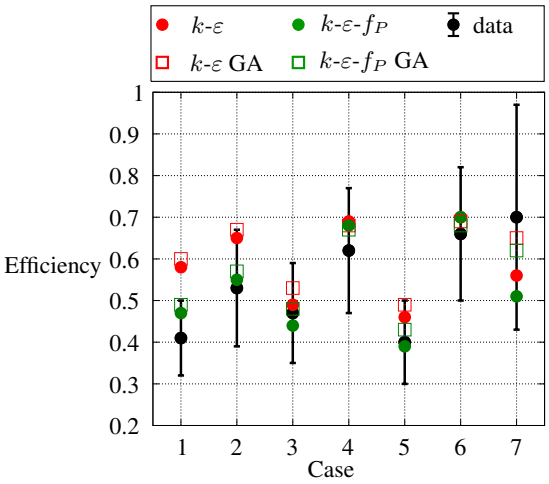

Figure 18. Wind farm efficiency for all test cases. Cases 1 and 2: Wieringermeer with low and high ambient turbulence intensity, Cases 3 and 5: Lillgrund with aligned wind directions, with 4.3D and 3.2D spacing. Cases 4 and 6: Lillgrund with staggered wind directions, with 4.3D and 3.2D spacing. Case 7: Horns Rev. Non-filled symbols are Gaussian Averaged (GA) results.

calculation corresponds to mostly wind directions with staggered configurations and the difference in power is negligible at the third or fourth wind turbine in a row.

3.2.5. Computational cost

The simulations are computed on a user-shared PC cluster that has eighty nodes with two Intel Xeon X5650 processors with six cores each. The clock frequency of a core is 2.66 GHz. The total number of CPU hours (number of CPUs $\times$ wall clock time) per wind direction is listed in Table VII and it is computed as an average of all simulated wind directions. The k-ε-f_P EVM needs more iterations than the k-ε EVM, especially for the case with aligned wind directions, which causes the difference in computational cost. However, the k-ε-f_P EVM is still three orders of magnitude cheaper compared to LES. For example, Churchfield et al. [24] performed LES of the Lillgrund wind farm that took approximately 1,000,000 CPU hours using 4096 cores to simulate only 10 minutes of realtime data for a single wind direction. It should be noted that Churchfield et al. used the actuator line technique [42], which requires a finer cell spacing than the AD method, and the time step is limited to the tip speed (Churchfield et al. used $D/53 = 1.75$ m and 0.015 s, respectively). If ADs are used, a significant reduction in computational cost can be achieved because a cell spacing of $D/30$ is required if the Reynolds-stresses in the wake need to be resolved, and even $D/15$ is enough if only the mean velocity deficit is desired [9]. In addition, the time step in a AD-LES is not limited to the tip speed, but it can be set to a Courant-Friedrichs-Lewy condition that is based on the free-stream velocity.

Table VII. Average computational effort in CPU hours per wind direction.

Case	Description	Cores	Cells	CPU k-ε	CPU k-ε-f_P
1-2	Wieringermeer	1×12	3.9×10^6	14	15
3-6	Lillgrund	6×12	2.4×10^7	250	309
7	Horns Rev	9×12	8.5×10^7	1043	1527

4. CONCLUSIONS

The performance of the k-ε EVM and the k-ε-f_P EVM is evaluated for seven test cases corresponding to three different wind farms: Wieringermeer, Lillgrund and Horns Rev. The wind direction uncertainty of the measurements is used to correct the model results with a Gaussian filter, such that a fairer comparison can be made between the measurements and simulations. For wind directions that are aligned with the wind turbine rows, the k-ε EVM underpredicts the power deficit at the second wind turbines in all cases, whereas the k-ε-f_P EVM shows comparable results with the measurements. Further downstream, at the third or fourth wind turbine in a row, the RANS turbulence models predict similar power deficits.

Wind Energ. 2014; **00**:1–20 © 2014 John Wiley & Sons, Ltd.
DOI: 10.1002/we
Prepared using weauth.cls

The two Wieringermeer cases imply that the effect of wake rotation on the power deficit is negligible. However, it is believed that the atmospheric stability does influence the power deficit, since the k-ε-f_P EVM is not able to predict the power deficit in Wieringermeer wind farm that is measured in stable atmospheric conditions.

The Horns Rev case shows that the effect of Gaussian averaging on the power deficit and wind farm efficiency is larger than the difference between k-ε EVM with the k-ε-f_P EVM. Hence, the choice of turbulence model is just as important as including the wind direction uncertainty in the post processing. Therefore, it is important to further investigate the methods that are used to estimate the wind direction uncertainty.

The difference in wind farm efficiency predicted by the k-ε EVM and the k-ε-f_P EVM becomes smaller for increasing wind turbine spacing and wind farm size. In addition, the difference between the prediction of the two models is small for wind directions that are misaligned with respect to the wind turbine rows. Hence, it is expected that the k-ε EVM and the k-ε-f_P EVM will predict similar values of the annual energy production for large wind farms with relatively large wind turbine spacing.

ACKNOWLEDGEMENTS

This work is supported by the Center for Computational Wind Turbine Aerodynamics and Atmospheric Turbulence funded by the Danish Council for Strategic Research, grant number 09-067216. Computational resources were provided by DCSC and the DTU central computing facility. The authors would like to acknowledge J.G. Schepers for providing the measurement data and feedback on the results of these measurements.

REFERENCES

1. Barthelmie RJ, Hansen K, Frandsen ST, Rathmann O, Schepers JG, Schlez W, Philips J, Rados K, Zervos A, Politis ES, *et al.*. Modelling and measuring flow and wind turbine wakes in large wind farms offshore. *Wind Energy* 2009; **12**:431–444.
2. Jensen LE. Array efficiency at Horns Rev and the effect of atmospheric stability. *EWEC, Milan, Italy*, 2007.
3. Jensen NO. A note on wind generator interaction. *Technical Report Risø-M-2411*, Risø National Laboratory, Roskilde, Denmark 1983.
4. Hansen KS. WP1 wake model performance validation results for Lillgrund offshore wind farm. *Technical Report*, EERA DTOC 2013.
5. Ott S, Nielsen M. Developments of the offshore wind turbine wake model Fuga. *Technical Report E-0046*, DTU Wind Energy, Denmark 2014.
6. Troldborg N, Larsen GC, Madsen HA, Hansen KS, Sørensen JN, Mikkelsen R. Numerical simulations of wake interaction between two wind turbines at various inflow conditions. *Wind Energy* 2011; **14**:859–876.
7. van der Laan MP, Sørensen NN, Réthoré PE, Mann J, Kelly MC, Troldborg N, Schepers JG, Machefaux E. An improved k-ε model applied to a wind turbine wake in atmospheric turbulence. *Wind Energy* 2014; Published online.
8. Mikkelsen R. Actuator Disc Methods Applied to Wind Turbines. PhD Thesis, Technical University of Denmark, Mek dept 2003.
9. van der Laan MP, Storey RC, Sørensen NN, Norris SE, Cater JE. A CFD code comparison of wind turbine wakes. *Journal of Physics: Conference Series 524, 012140*, 2014.
10. Réthoré PE. Wind Turbine Wake in Atmospheric Turbulence. PhD Thesis, Risø 2009.
11. El Kasmi A, Masson C. An extended k-ε model for turbulent flow through horizontal-axis wind turbines. *Journal of Wind Engineering and Industrial Aerodynamics* 2008; **96**:103–122.
12. Prospathopoulos JM, Politis ES, Rados KG, Chaviaropoulos PK. Evaluation of the effects of turbulence model enhancements on wind turbine wake predictions. *Wind Energy* 2011; **14**:285–300.
13. Cabezón D, Migoya E, Crespo A. Comparison of turbulence models for the computational fluid dynamics simulation of wind turbine wakes in the atmospheric boundary layer. *Wind Energy* 2011; **14**:909–921.
14. van der Laan MP, Sørensen NN, Réthoré PE, Mann J, Kelly MC, Troldborg N. The k-ε-f_p model applied to double wind turbine wakes using different actuator disk force methods. *Wind Energy* 2014; Submitted in March.
15. Panofsky HA, Dutton JA. *Atmospheric Turbulence*. Wiley-interscience, New York, US, 1984.
16. Schepers JG, Obdam TS, Prospathopoulos J. Analysis of wake measurements from the ECN Wind Turbine Test Site Wieringermeer, EWTW. *Wind Energy* 2012; **15**:575–591.
17. Lindenburg C, Snel H. PHATAS-II: program for horizontal axis wind turbine analysis and simulation version II. *Technical Report*, ECN-C–93-038 1993.
18. Schepers JG. Personal communication 2012; .

19. Hansen KS, Barthelmie RJ, Jensen LE, Sommer A. The impact of turbulence intensity and atmospheric stability on power deficits due to wind turbine wakes at Horns Rev wind farm. *Wind Energy* 2012; **15**:183–196.
20. Kelly MC, Gryning SE. Long-term mean wind profiles based on similarity theory. *Boundary-Layer Meteorology* 2010; **136**:377–390.
21. Sathe A, Gryning SE, Peña A. Comparison of the atmospheric stability and wind profiles at two wind farm sites over a long marine fetch in the North Sea. *Wind Energy* 2011; **14**:767–780.
22. Dahlberg JÅ. Assessment of the Lillgrund windfarm. *Technical Report*, Vattenfall Vindkraft AB 2009.
23. Hansen KS. Presentation of Lillgrund offshore wind farm and the Siemens SWT-2.3-93 wind turbine. *Technical Report*, EERA DTOC 2013.
24. Churchfield MJ, Lee S, Moriarty PJ, Martinez LA, Leonardi S, Vijayakumar G, Brasseur JG. A Large-Eddy Simulation of Wind-Plant Aerodynamics. *AIAA Conference, Nashville, USA*, 2012.
25. Barthelmie RJ, Frandsen ST, Rathmann O, Hansen K, Politis ES, Prospathopoulos J, Schepers JG, Rados K, Cabezón D, Schlez W, *et al.*. Flow and wakes in large wind farms: Final report for UpWind WP8. *Technical Report Risø-R-1765*, Risø 2011.
26. Bergström H. Meteorological Conditions at Lillgrund. *Technical Report*, Vattenfall Vindkraft AB 2009.
27. Sørensen NN. General purpose flow solver applied to flow over hills. PhD Thesis, Technical University of Denmark 1994.
28. Michelsen JA. Basis3d - a platform for development of multiblock PDE solvers. *Technical Report AFM 92-05*, Technical University of Denmark, Lyngby 1992.
29. Patankar SV, Spalding DB. A calculation procedure for heat, mass and momentum transfer in three-dimensional parabolic flows. *International Journal of Heat and Mass Transfer* 1972; **15**:1787–1806.
30. Leonard BP. A stable and accurate convective modelling procedure based on quadratic upstream interpolation. *Computer Methods in Applied Mechanics and Engineering* 1979; **19**:59–98.
31. Réthoré PE, Sørensen NN. A discrete force allocation algorithm for modelling wind turbines in computational fluid dynamics. *Wind Energy* 2012; **15**:915–926.
32. Rhie CM, Chow WL. Numerical study of the turbulent fow past an airfoil with trailing edge separation. *AIAA Journal* 1983; **21**:1525–1532.
33. Sørensen NN, Bechmann A, Johansen J, Myllerup L, Botha P, Vinther S, Nielsen BS. Identification of severe wind conditions using a Reynolds Averaged Navier-Stokes solver. *Journal of Physics: Conference series 75, 012053*, 2007.
34. van der Laan MP, Sørensen NN, Réthoré PE, Mann J, Kelly MC, Schepers JG. Nonlinear Eddy Viscosity Models applied to Wind Turbine Wakes. *Proceedings for the ICOWES2013, Copenhagen, Denmark*, 2013; 514–525.
35. Launder BE, Spalding DB. *Mathematical models of turbulence*. Academic Press, London, UK, 1972.
36. Boussinesq MJ. *Théorie de l'écoulement tourbillonnant et tumultueux des liquides*. Gauthier-Villars et fils, Paris, France, 1897.
37. Richards PJ, Hoxey RP. Appropriate boundary conditions for computational wind engineering models using the k-ε turbulence model. *Journal of Wind Engineering and Industrial Aerodynamics* 1993; **46,47**:145–153.
38. Réthoré PE, van der Laan MP, Troldborg N, Zahle F, Sørensen NN. Verification and validation of an actuator disc model. *Wind Energy* 2014; **17**:919–937.
39. Troldborg N, Zahle F, Sørensen NN, Réthoré PE. Comparison of wind turbine wake properties in non-sheared inflow predicted by different CFD rotor models. *Wind Energy* 2014; Published online.
40. Gaumond M, Réthoré PE, Ott S, Peña A, Bechmann A, Hansen KS. Evaluation of the wind direction uncertainty and its impact on wake modeling at the Horns Rev offshore wind farm. *Wind Energy* 2013; Published online.
41. Wu YT, Porté-Agel F. Modeling turbine wakes and power losses within a wind farm using LES: An application to the Horns Rev offshore wind farm. *Proceeding for the ICOWES2013, Copenhagen, Denmark*, 2013; 537–548.
42. Sørensen JN, Shen WZ. Numerical modelling of wind turbine wakes. *Journal of Fluids Engineering* 2002; **124**:393–399.

DOI: 10.1002/we
Prepared using weauth.cls